



Higgins, R. J. , Barakos, G. N. , Shahpar, S. and Tristante, I. (2021) A computational fluid dynamic acoustic investigation of a tiltwing eVTOL concept aircraft. *Aerospace Science and Technology*, 111, 106571. (doi: [10.1016/j.ast.2021.106571](https://doi.org/10.1016/j.ast.2021.106571))

The material cannot be used for any other purpose without further permission of the publisher and is for private use only.

There may be differences between this version and the published version. You are advised to consult the publisher's version if you wish to cite from it.

<http://eprints.gla.ac.uk/233863/>

Deposited on 10 February 2021

Enlighten – Research publications by members of the University of
Glasgow

<http://eprints.gla.ac.uk>

A Computational Fluid Dynamic Acoustic Investigation of a Tiltwing eVTOL Concept Aircraft

Ross J. Higgins¹, George N. Barakos²

University of Glasgow, James Watt South Building, Glasgow, G12 8QQ, U.K.

Shahrokh Shahpar³, Indi Tristante⁴

Rolls-Royce plc., Derby, DE24 8BJ, U.K.

Abstract

With the advancement in electric propulsion systems, aircraft designers and manufacturers are no longer constrained to established configurations. Developments in Vertical Take-off and Landing (VTOL) aircraft have been seen in recent times through the design of modern tiltrotor aircraft, tiltwing concepts and multi-rotor designs. The combination of these developments allowed engineers to propose designs which utilise the vertical take-off and landing capabilities of a tiltrotor aircraft with electrically driven propulsion systems, deemed eVTOL (Electrically driven Vertical Take-off and Landing). This investigation aims to develop an understanding of the aeroacoustic emissions associated with the non-linear interaction resulting from multi-rotor integrated propellers and a tiltwing eVTOL airframe. Acoustics is one of the key requirements of any future eVTOL aircraft certification, hence, an investigation was conducted into the baseline design, followed by an optimisation study aiming to reduce the amount of noise generated.

Keywords: eVTOL, Aeroacoustics, CFD, Propeller Synchronising

¹Research Assistant, CFD Laboratory.

²Professor, CFD Laboratory, corresponding author.

³RR Engineering Fellow, Aerothermal Design System, Innovation Hub, Future Methods

⁴Innovation Hub, Future Methods

Nomenclature

Latin symbols

c_{ref}	Reference chord (m)
k	Turbulence Kinetic Energy (m^2/s^2)
n_b	Number of blades per propeller (-)
n_p	Number of propellers (-)
p_{ref}	Reference acoustic pressure (Pa)
p'	Acoustic pressure (Pa)
\mathbf{R}	Vector of the flux residual
S	Wing Span (m)
t	Time (s)
V	Cell volume
\mathbf{W}	Vector of conservative variables
x	Space (m)
Y^+	Non-dimensional wall distance (-)

Greek symbols

ψ_{max}	Maximum synchrophasing phase shift ($^\circ$)
ω	Specific Rate of Dissipation (1/s)
λ	Non-dimensional Propeller BPF Wavelength (c_{ref})

Acronym

BILU	Block Incomplete Lower-Upper
BPF	Blade Passing Frequency
CFD	Computational Fluid Dynamics

CFL	Courant-Friedrichs-Lewy
DDES	Delayed-Detached Eddy Simulation
DES	Detached Eddy Simulation
eVTOL	Electrical Vertical Take-Off/Landing
HMB3	Helicopter-Multi-Block 3
IMPACTA	Improving the Propulsion Aerodynamic and acoustics of Turboprop Aircraft
JORP	Joint Open Rotor Propeller
LES	Large Eddy Simulation
MUSCL	Monotone Upstream-centred Schemes for Conservation Laws
OSPL	Overall Sound Pressure Level (dB)
RANS	Reynolds-Averaged Navier-Stokes
RK4	4 stage Runge-Kutta
SAS	Scale Adaptive Simulation
SBES	Stress-Blended Eddy-Simulation
URANS	Unsteady Reynolds-Averaged Navier-Stokes
VTOL	Vertical Take-Off/Landing

1. Introduction

With the advancement in the design of electric batteries [1], designers and manufacturers are no longer constrained to standard aircraft designs. These designs no longer have to include the carbon-fuel based propulsion systems of typical aircraft as they now have the potential to benefit from environmentally friendly electric systems. Developments in Vertical Take-off and Landing (VTOL) aircraft have also been seen in recent times through the design of modern tiltrotor aircraft such as the AW609 (Figure 1(a)).

The combination of these developments has allowed engineers to develop designs which utilise the vertical take-off and landing capabilities of a tiltrotor



Figure 1: Previous tiltrotor and tiltwing aircraft designs

aircraft with electrically driven propulsion systems, deemed eVTOL (Electrically driven Vertical Take-off and Landing) [2].

The possibility of an electric propulsion system has also made it possible to revisit the tiltwing concept that was demonstrated in the XC-142 (Figure 1(b)). Cross-shafting can be achieved by simpler electrical connection between motors. This combination is seen as a key enabler in a new dimension of aerospace research which focuses on light flying machines suitable for air-taxi operations which work in conjunction with current urban transport systems.

Such a concept has been developed by Rolls-Royce and is presented in Figure 2. This concept was unveiled by Rolls-Royce in 2018 and utilises multi-rotor electrically-driven propulsion with a tiltwing airframe [3, 4]. The idea behind the concept is to use the tiltwing capability with the front propellers to vertically take-off/land. The front propellers would then be folded following the completion of the transition phase.

One of the key challenges associated with an electrically driven multi-rotor aircraft design is its aeroacoustic emissions. New European regulations are to be introduced in 2020 which aims to reduce the acoustic footprint of aircraft by 50% [5], with a total noise abatement of 65% by 2050 [6]. As a result of this, an investigation is required to understand and reduce the amount of noise generated by the eVTOL concept aircraft.

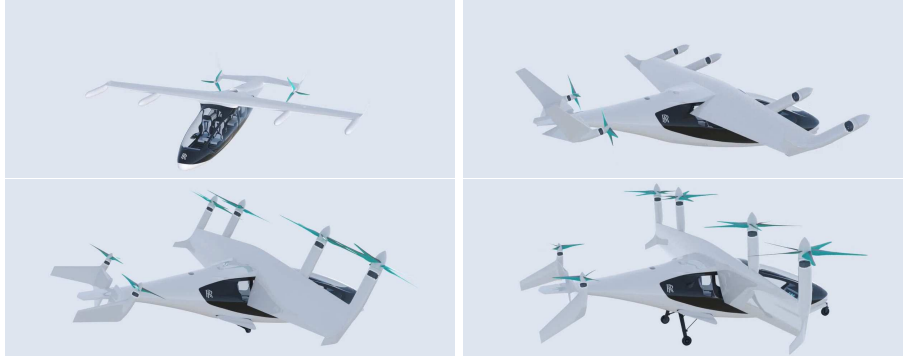


Figure 2: Rolls-Royce eVTOL tiltwing concept aircraft in transition from hover to forward-flight

In terms of noise predictions, empirical methods with non-linear corrections are still utilised today. Such empirical models include those described by Magliozzi [7], Smith [8] and Dobrzynski [9]. Although such models can be deemed to provide accurate solutions, the dominating non-linearity associated with a multi-rotor eVTOL design requires higher-fidelity methods, such as Navier-Stokes based fluid dynamics.

The use of Computational Fluid Dynamics (CFD) for the study of aeroacoustics has advanced in recent years through the increase in computing power and the introduction of high-order upwind schemes to reduce numerical dissipation [10, 11]. In addition to this, the use of scale-resolving methods have become widely used to assess both the broadband and tonal noise components. This includes Delayed-Detached-Eddy-Simulation (DDES) [12], Large-Eddy-Simulation (LES) [13] and Stress-Blended Eddy-Simulation (SBES) [14]. Such studies focus on compressor test cases [13, 14] and therefore, differences between internal and external rotor flows must be taken into consideration.

More fundamental studies focusing on aerofoil designs have also been conducted using CFD and include the use of scale-resolving methods [12]. The design of the aerofoil can have a significant impact on the noise emissions and

factors such as aerofoil thickness, angle of attack and camber have previously been studied [15]. However, such studies negate the three-dimensional influence of a propeller/rotor flow and therefore, comprehensive studies must be conducted. Such studies involve those conducted using HECTOR [16] and ONERA free/prescribed wake methods [17]. Although such methods can provide accurate solutions for given configurations, the complex and non-linear nature of the eVTOL aircraft requires higher-fidelity Navier-Stokes based CFD.

As a result, this investigation will utilise CFD in order to assess the aeroacoustics **both on and off body**. As the aircraft is designed for urban commuters, the understanding of the acoustics to a ground observer is required along with the fluctuations around the cabin.

2. Numerical Methods

For this investigation, the in-house CFD solver Helicopter-Multi-Block-3 (HMB3) is used. The core functionality of HMB3 is CFD, with its use extended in recent years to include whole engineering applications, including helicopter rotor aeroelasticity [18], propeller aeroacoustics [19], flight mechanics [20] and missile trajectory prediction [21]. Further detail on the numerical schemes and methods can be found in the referenced articles.

HMB is capable of modelling turbulence from the higher-order techniques to the one-equation turbulence models closing the Reynolds-Averaged Navier-Stokes (RANS) equations. The higher-order techniques are required to capture the broadband noise associated with propeller flow. However, due to fact tonal noise is the main source of acoustics for this aircraft, the two-equation $k - \omega$ turbulence model [22] is used to close the Unsteady RANS (URANS) equations. This turbulence model is selected not only for tonal noise estimations, but also to ensure efficient calculations.

The $k - \omega$ turbulence model has been proven over a variety of validation investigations to provide both accuracy and efficiency. These investigations using HMB3 have included propeller flow validation in both installed and isolated conditions, by comparison with the experimental results of the Joint Open Rotor Propeller (JORP) blade [23], the Improving the Propulsion Aerodynamic and acoustics of Turboprop Aircraft (IMPACTA) wind tunnel tests [24, 25] and the model aircraft propeller inflow investigation at the University of Glasgow [26]. Good agreement in terms of aerodynamics, acoustics and aeroelasticity were seen by all [27, 28, 29, 30].

Due to the design nature of the eVTOL aircraft, the validation of multiple flight regimes must be verified before any attempt is made to simulate a select configuration. With this in mind, HMB3 was also been validated for tiltrotors. The validation involves the simulation of the AW609/ERICA tiltrotor to experiment and additional CFD results [31, 32], along with a study on the XV-15 tiltrotor blade [32]. This is encouraging as tiltrotors are similar in their design scope to the selected eVTOL aircraft. This, therefore, ensures confidence in the method to simulate such a configuration.

As part of the investigation into the full simulation of a tiltrotor aircraft, a higher-order (up to 4th-order) MUSCL scheme was implemented in order to improve the wake resolution and acoustic predictions for rotorcraft applications [11]. A Fourier analysis was conducted to assess the spectral properties of the proposed scheme with a comparison made to the baseline (2nd order) upwind scheme for the dispersion and dissipation. Both perform well across a range of wavenumbers with a reduction in the dissipation found for the 4th order scheme. As this investigation is mainly focused on near-field acoustic predictions with multiple chimera interpolations, a nominally assessed 3rd order scheme is used for robustness. This order of accuracy is expected to drop to 2nd order at the

far-field boundaries due to the coarse nature of the grid at such extremes.

The noise estimations are calculated based upon the pressure profiles from the CFD solutions. The unsteady pressure field ($p'(x, t)$) is determined based upon the subtraction of the propeller revolution average value from the raw solution. This is then used along with a reference value (p_{ref}) of $2 \times 10^{-5} Pa$ to calculate the Overall Sound Pressure Level (OSPL) presented in Equation 1.

$$OSPL = 10 \log_{10} \left(\frac{p_{rms}^2}{p_{ref}^2} \right) dB \quad (1)$$

Multi-block structured meshes are used with HMB3, which allow an easy sharing of the calculation load for parallel simulations. ICEM-HexaTM of ANSYS is used to generate the mesh. An overset grid method is available in HMB3 [33], to allow for relative motions between mesh components. The chimera method is based on composite grids, consisting of independently generated, overlapping non-matching sub-domains, hence simplifying the mesh generation. Each of these sub-domains are referred to as a *levels* and are sorted hierarchically, with higher *levels* having priority. The exchange of information between sub-domains is achieved through conservative interpolation of fluxes and by following the hierarchy of mesh *levels* [33]. Such *levels* and grid information is presented in Section 3.1.

3. Baseline eVTOL Aircraft

The key focus of this investigation involves the simulation of the full Rolls-Royce aircraft for acoustic emissions using the HMB3 CFD solver. Focus was initially placed on the the simulation of the aircraft during hover flight, with a transition to forward flight following the completion of the hover simulations.

3.1. Grid Generation

The chimera grid method is used for the full aircraft. This allows individual component of the aircraft to be meshed within its own sub-domain. A total of five chimera *levels* are used and these include the blades, main/tail wing and fuselage. An additional circular drum *level* between the blades and main/tail wings is introduced to improve the interpolation.

Table 4 details the grid size and chimera *level* for each sub-domain for the semi-span aircraft simulations in hover and forward flight. The largest individual sub-domain is the fuselage grid in both hover and forward flight. This is to ensure enough cells are present around both the tail and wing to ensure sufficient interpolation. In forward flight the front propeller blades are folded, hence these grids and the front drum are not required for this test condition. A spacing of $1 \times 10^{-6} c_{ref}$ is applied to the cells normal to all solid surfaces. This ensures the required Y^+ value to be less than 1.0 for the resolution of the viscous sub-layer in the $k - \omega$ turbulence model. [Given our earlier work on twin-engine turbo-props \[34\]](#), the mesh resolution presented in Table 4 is seen to be adequate for resolving the tonal noise component both on and off-body, which is our main concern. [In addition, we are looking at differences between cases instead of absolute values.](#)

Presented in Figure 3 is the visualisation of the computational domain and chimera boundaries for the key components. The size of the domain does not change between hover and forward flight, with [freestream](#) far-field boundary conditions applied to the extreme background faces. Non-reflecting far-field boundaries were [not](#) applied to reduce the computational complexity and [because](#) the background grid becomes significantly coarse towards the extreme faces. [Furthermore, the non-reflecting boundaries can add to the stiffness and complexity of this full aircraft simulation.](#) The resolved acoustic extraction is

Grid Component	Hover		Forward Flight	
	Grid Size	<i>Level</i>	Grid Size	<i>Level</i>
Background	12,250,000	1	12,250,000	1
Fuselage	26,654,587	2	28,663,627	2
Wing	20,853,912	3	17,441,402	3
Tail	13,077,920	3	12,712,160	3
Front Drum	9,313,504	4	<i>n/a</i>	-
Rear Drum	3,672,000	4	3,672,000	4
Front Propellers	3,911,100 <i>x2</i>	5	<i>n/a</i>	-
Rear Propellers	5,023,188	5	5,023,188	5
Total	98,667,311	-	79,762,377	-

Table 4: Grid summary for the semi-span aircraft in hover and forward flight

not influenced by these boundary conditions due to the extreme distances from the boundaries (see Figure 4).

The topology used for the wing and tail in forward flight is adjusted to ensure sufficient interpolation between these components and the lower *level* fuselage grid. The adjustments are focused on the removal of blocks around wing/tail-fuselage junctions which are found to be inside a solid wall of a lower *level*.

Due to the size of the computational grid, the storing of large flow-field solutions can be problematic. Therefore, numerical probes are inserted into the grid to ensure the flow-field solution can be stored at several locations at each time-step. A numerical plane, consisting of an array of probes, is used for this simulation in order to insert a fictitious ground plane. The ground plane is located 16.5 non-dimensional propeller BPF wavelengths (λ) vertically downstream of the aircraft with a width and length of 27.5λ and 38.5λ , respec-

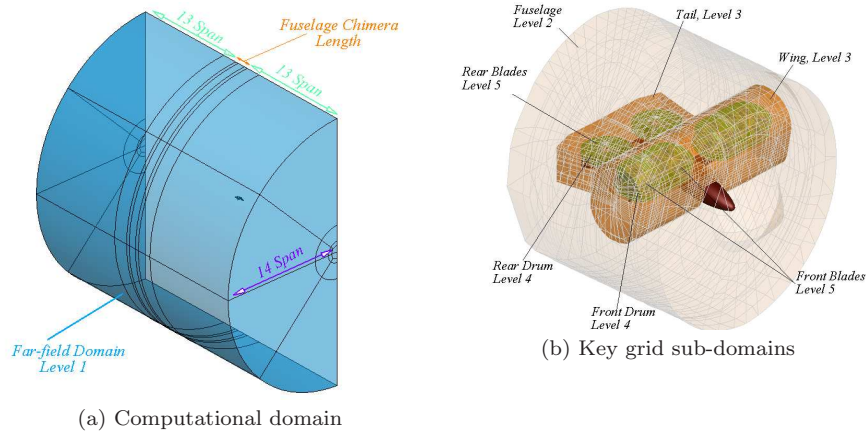


Figure 3: eVTOL aircraft chimera grid in hover

tively. This equates to an approximate distance of 3 span-lengths (S) vertically downstream of the aircraft, with the freestream far-field boundary conditions a further 11 S (or 60.5λ) away. Such a distance, along with the coarsening of the grid, ensures there is no reflection of far-field acoustics affecting the fictitious ground plane.

A total of 1043 probes are used across this plane. The fictitious ground probes are converted into a surface and presented in Figure 4(a). This surface represents a coarse plane of the flow-field grid and therefore some higher frequency content may be missed via the probes. The probes will be able to capture the overall trend and magnitude of the aircraft acoustics. Such a plane allows for the initial observations of the noise emissions to a ground observer to be determined without the reflection typically associated with a solid wall.

In addition to the ground plane, the flow-field solution is examined via a variety of planes and these are presented in Figures 4(b)-(e). These planes aim to capture the vertical, lateral and horizontal directivity of the sound waves. Planes AF and AR (Figures 4(b) and (c), respectively) represent axial planes vertically downstream of the front and rear propellers. Due to the change in vertical location between the front and rear propellers, and the forward rotation

of the main wing, a single plane could not be used. These planes therefore capture the sound waves directly underneath the propellers.

To capture the full acoustic picture, vertical planes at the wing and tail pivot points are utilised and these are presented in Figures 4(d) and (e), respectively. These are captioned planes VF and VR representing the front and rear propeller influence. In a similar manner to the ground probes, some higher frequency content may be missing from the plane signals. This is due to the fact that such planes are taken from the flow-fields which are written every 3° of the propeller rotation. However, assuming the waves travel at a speed of sound at $20^\circ C$ in air and the blade passing frequency of the front propeller, a non-dimensional wavelength of $\sim 18 c_{ref}$ is found and this relates to ~ 100 cells per wavelength within the near-field plane and ~ 3 cells per wavelength for the ground plane.

3.2. Simulation Setup

With the semi-span grid defined, the following section will detail the test conditions for the simulation of the aircraft in hover and forward flight using the Unsteady Reynolds-Averaged Navier-Stokes (URANS) equations with the baseline $k - \omega$ turbulence model.

Presented below in Table 5 is the test conditions simulated using HMB3 in hover. As the simulation will be conducted in hover with zero freestream velocity, the reference velocity for the Mach and Reynolds number is taken as the front blade tip velocity. The front blade root chord is also used as the reference length.

Presented below in Table 6 is the test conditions simulated using HMB3 in forward flight. The reference chord length is kept constant with the reference Mach and Reynolds numbers adjusted to the freestream velocity conditions. The propeller rotational velocity is applied via the rigid body rotation with an updated reduced frequency required based upon the tip and freestream veloci-

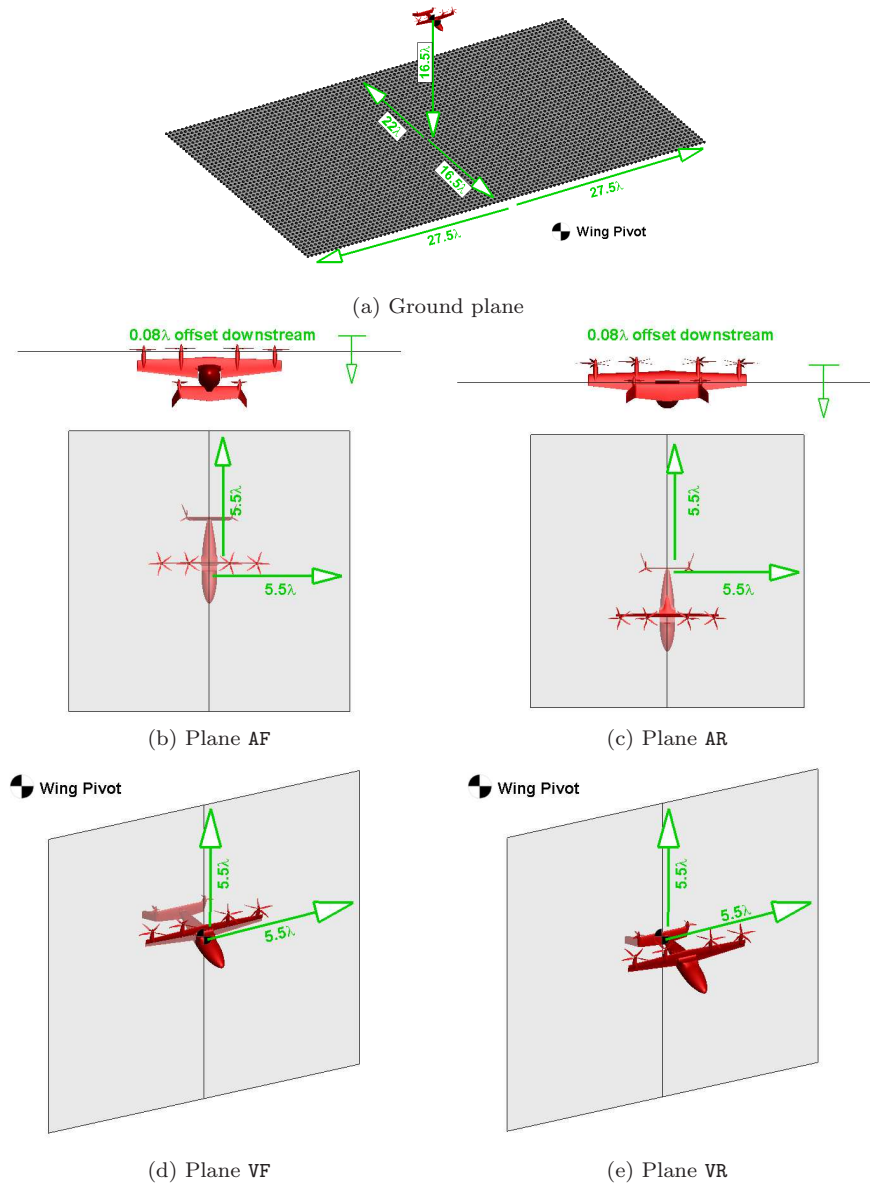


Figure 4: Flow-field visualisation locations for both hover and forward flight simulations

ties.

For both hover and forward-flight, the counter rotation of the propeller

Reference Reynolds Number (-)	$\sim 2 \times 10^6$
Reference Mach Number (-)	~ 0.6
Freestream Velocity (m/s)	0.0
Ambient Conditions	<i>ISA Sea-level</i>
Simulation Method	<i>URANS</i>
Turbulence Modelling	<i>k - ω</i>

Table 5: Summary of the test conditions for the semi-span aircraft in hover.

blades, between the starboard and port sides, was kept constant throughout the simulations. The counter rotation was selected based upon past experience with turbo-prop aircraft [34] and the design of the A400 Atlas. A full optimisation study of the propeller rotation for this configuration would be required for both aeroacoustics and aerodynamics.

Reference Reynolds Number (-)	$\sim 0.4 \times 10^6$
Reference Mach Number (-)	~ 0.12
Ambient Conditions	<i>ISA Sea-level</i>
Simulation Method	<i>URANS</i>
Turbulence Modelling	<i>k - ω</i>

Table 6: Summary of the test conditions for the semi-span aircraft in forward flight.

3.3. Results of the baseline eVTOL aircraft in hover and forward flight

Presented in Figure 5 is the instantaneous Overall Sound Pressure Level (OSPL) for the aircraft in hover and forward flight. The raw scale has been removed for confidentiality, with the difference in contour levels representing 7 dB. Comparing both flight conditions, a reduction in OSPL is seen across the aircraft surface when in forward flight. This is expected based upon the

folding of the front propellers, and thus reducing the number of noise sources. Looking at average values, there is a reduction in the noise level from hover to forward-flight of ~ 14 dB.

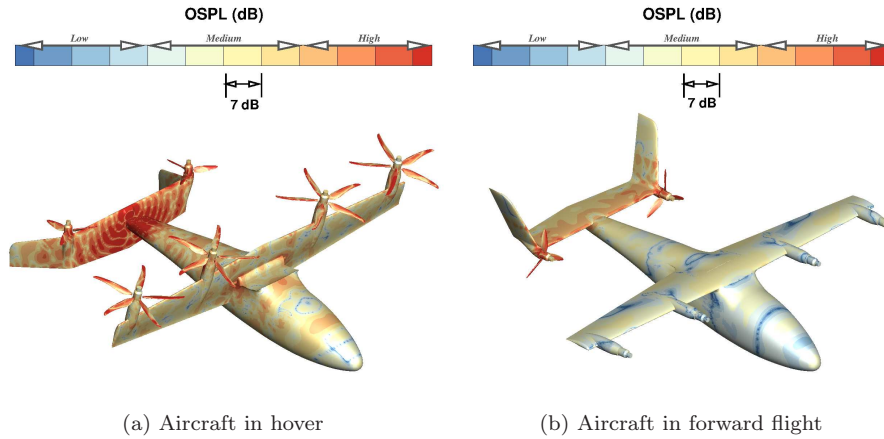


Figure 5: Instantaneous surface overall sound pressure level (OSPL) for the aircraft in hover and forward flight

For both flight conditions, the propeller blades are seen as the main source of high level noise across the surface. The interaction with the fixed components of the aircraft introduce secondary effects. Focusing on the aircraft in hover (Figure 5(a)), the propeller wake fluctuations are seen across the lower surface of the wing and tail. For the front propeller, this wake propagates towards the fuselage-wing junction creating a secondary noise source at this location and this travels across the fuselage, both forward and aft. The forward propagation increases the noise levels for the passengers and contributes to the ~ 14 dB difference between the flight conditions. In a similar manner to the front propeller wake, the acoustic waves generated from the rear blades are directed towards the centre of the aircraft. These subsequently interact with the aft travelling fuselage-wing junction waves creating the high frequency and high noise level acoustics seen across the tail.

In terms of the forward flight results (Figure 5(b)), the high level acoustics

are contained to the rear of the aircraft. The acoustic fluctuations are found across both the vertical and horizontal stations of the tail. Although such fluctuations are high in comparison to the rest of the airframe, the high frequency oscillations observed in hover are no longer present. This is due to the folding of the front propellers, the position of the tail and wing, and subsequently, the stabilising freestream velocity. The acoustic waves driven from the rear propellers are weaker across the fuselage and wing.

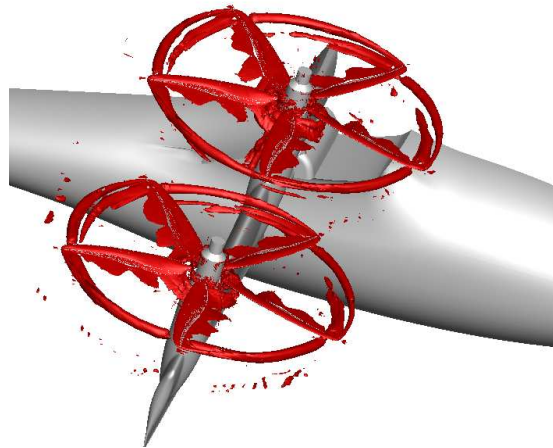


Figure 6: Front propeller blade vortex interaction for the aircraft in hover visualised via iso-surfaces of Q -criteria

In hover, some of the highest values of OSPL are seen at the front propeller blades. This correlates with the high thrust coefficient produced by each blade. Furthermore, it is also influenced by a significant blade vortex interaction. The blade-to-blade interaction is highlighted in Figure 6, where the tip vortex of the blade in-front impinges on the following blade. This occurs over the majority of the revolution, except during the phase in which the blade passes the centre section of the wing. This is also where the blade thrust is at its lowest. The reduction in thrust results in a reduction of the tip vortex strength, thus allowing it to pass under the following blade.

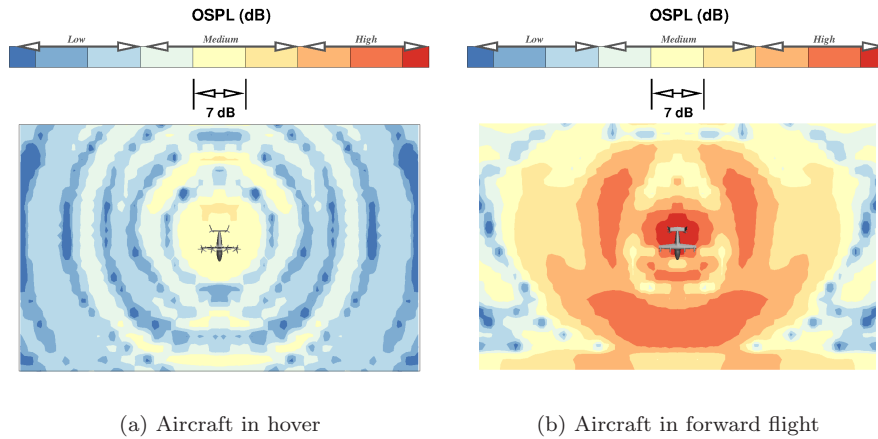


Figure 7: Average overall sound pressure level for the ground probes in both hover and forward flight

Presented in Figure 7 is the revolution average OSPL for the fictitious ground plane. A significant difference in the sound pattern is observed between the two flight conditions. High-frequency medium-level acoustics waves are seen underneath the aircraft in hover. This is potentially detrimental to the ground observer comfort as lower frequency tones are seen to be more comfortable to the human ear. In addition, the aircraft is likely to be present above a given location for a long period of time in comparison to the forward flight. Lower-frequency, high-level acoustics are captured within the ground probes of the forward flight simulation. Although an increase in noise level is captured, the short time period and low frequency will potentially see a reduced level of discomfort for the ground observer.

4. Synchrophasing Analysis

The optimisation of propeller acoustics is often driven by the aerodynamic optimisation of the given blades. Significant passive optimisations, such as the shape changes made to the IMPACTA propeller [19], may be beneficial to investigate during the design process. However, with the required multi-scope

operation of the eVTOL aircraft, a more active optimisation may be required to ensure optimal performance over the flight regime. These active optimisations have been studied in the past by HMB3 and involve dynamic blade twist [35], active chord modification [36] and the introduction of a Gurney flap [37]. All three techniques were found to derive performance enhancements, with the development of active twist, in particular, advanced due to the development of piezoelectric technology [38]. In addition to the specific blade design, optimisation of the airframe itself may result in aeroacoustic reductions. Such a study was conducted using HMB3 and focused on the design of the rear of the helicopter cabin [39]. Such optimisations involve significant computational cost, and combined with the use of the full airframe, are out of the scope of the current investigation. This leads to the desire to introduce propeller synchronising.

The technique of propeller synchronising is introduced to the eVTOL aircraft in order to mitigate the acoustics emissions. Synchronising involves the introduction of a phase shift between propellers, with past studies shown to have a positive benefit [34] for a twin-engine turbo-prop aircraft. The use of synchronising is seen as a cheap solution to the aeroacoustic problem due to the fact no significant addition to the aircraft system is required. In particular, eVTOL aircraft have an advantage over traditional gas turbine engines as the electric motor can be utilised to adjust the propeller phase. For a gas-turbine engine, additional hardware is required to introduce the phase difference. With this, and the inclusion of microphones at key stations around the aircraft, a simple optimiser can be used to find the ideal phase shift which reduces the noise levels for the aircraft passengers. Therefore, in order to assess this technique, a binary test on the eVTOL aircraft is conducted.

As the blade loads mirror the acoustic emissions, an estimate for the phase shift can be determined by assuming a pure sinusoidal profile for the blade

thrust. Aiming to ensure the blade loads are out-of-phase, the maximum phase shift (ψ_{max}) for a given propeller configuration is determined from Equation 2. This takes into account the number of propellers and blades across a single wing-like component. Further complexities, such as the port/starboard positioning and wing design, will require further consideration and hence, the true optimal phase angle can only be determined via onboard installation.

$$\psi_{max} = \frac{360}{n_b n_p} \quad (2)$$

Using Equation 2 as reference, the proposed synchrophasing configuration for the eVTOL aircraft is presented in Figure 8. In hover flight, a total of 12° phase shift is introduced between inner and outer front propellers with a 6° shift between port and starboard equivalent propellers. Due to the 110° angle between the horizontal and vertical sections of the tail, care had to be taken when adjusted the rear propeller angles. A shift of 27.5° and 82.5° on the starboard and port sides, respectively, will allow for the load oscillations at the rear to occur out-of-phase.

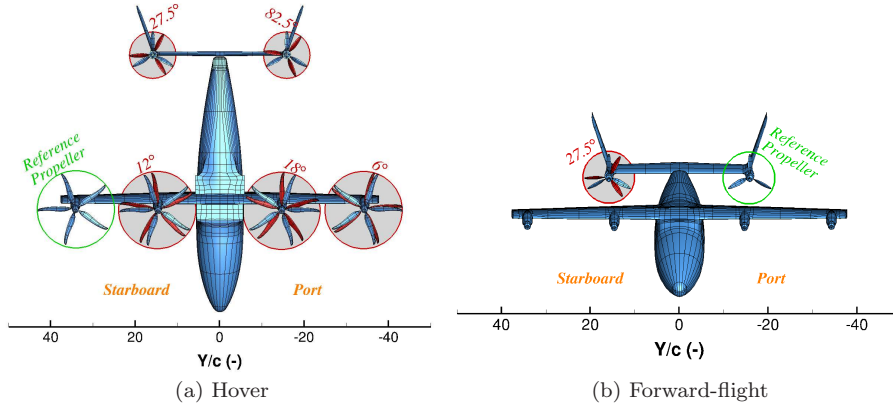


Figure 8: Synchrophasing schematic

Due to the folding of the front propellers in forward flight, only the rear

propeller blades have to be adjusted. Using the port propeller as the reference, the starboard propeller is shifted by 27.5° . This phase shift results in the starboard propeller being in-between the vertical and horizontal tail components as the port side is crossing the tail. The aim of this synchrophasing configuration is to ensure the periodic oscillation in blade loads only occurs in one blade at a given instance in time.

Due to the lack of symmetry in the propeller phase, synchrophased simulations required the full aircraft geometry. The same conditions as the semi-span aircraft is selected (Tables 5 & 6).

4.1. Results of the Synchrophased Aircraft in Hover

Presented in Figure 9 is the averaged overall sound pressure level for the synchrophased configuration and the difference between the two configurations on the AF and AR planes. For the averaged noise level (Figures 9(a) & (c)), the highest values for the synchrophased configuration appear downstream of the propellers. This is expected as these planes are extracted directly underneath the front and rear propellers, respectively. For the rear plane (AR), the regions of high noise level, are almost circular, and show an almost constant value around the azimuth and along the radius (except at the closest root section where the flow interacts with the nacelle). This suggests that the lifting profile of each blade is almost constant along the span with a high amount of blade twist. This is not seen for the front plane (AF) where the highest noise levels are contained around the blade tip indicating a more tip-wise lifting profile. In addition to this observation, there is a discrepancy between the maximum noise level underneath the inner and outer propellers on both port/starboard sides. This is due to the blade loads where a greater amount of thrust is generated by the outer blades thus producing higher noise levels.

Apart from the high value noise levels, medium level regions are seen around

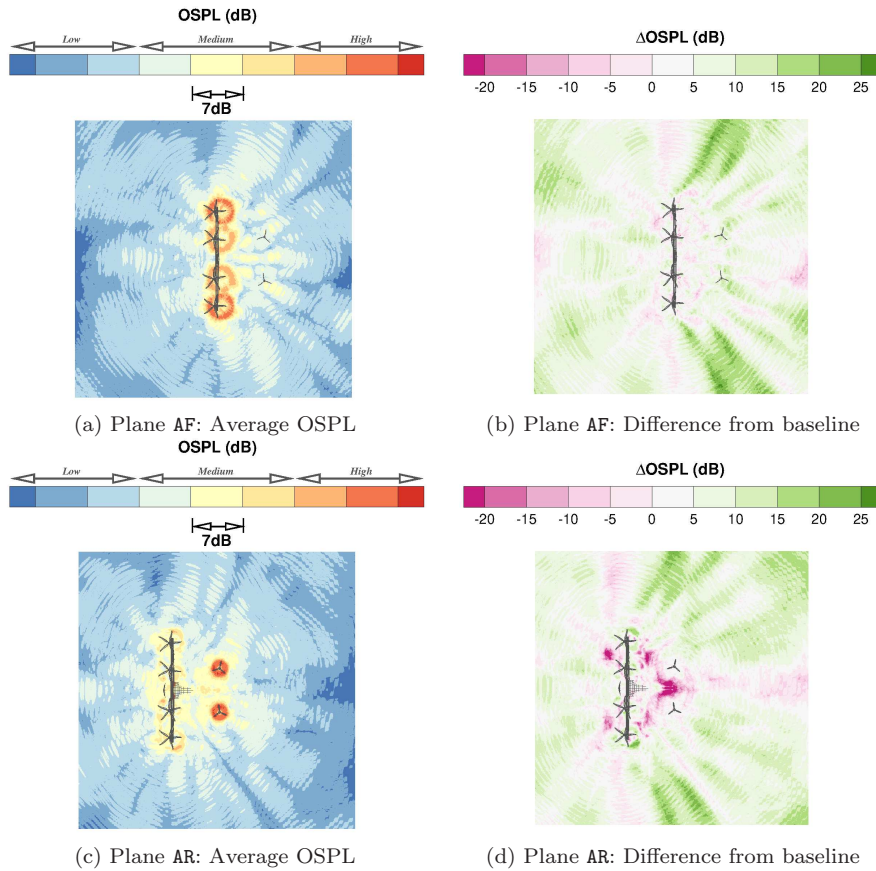


Figure 9: The average overall sound pressure level (OSPL) for the synchrophased configuration with the difference between the two configurations for the AF and AR planes in hover

the aircraft. For the front plane (AF) these are located $\sim 30^\circ$ aft of the outer propeller plane on both port/starboard side and also towards the rear of the aircraft $\sim 20^\circ$ outwards of the lateral plane at the rear propellers. The latter is a result of the interaction between the front and rear propeller waves, with this region also seen on the rear plane (AR) at a slightly different angle to the lateral plane. In addition to this for the rear plane, medium value noise levels are found in the centre of the aircraft between the two rear propellers. This was also seen on the baseline configuration where the sound waves generated from the fuselage-wing junction would propagate rearwards and interact with the

high noise level waves produced via the rear blades, thus creating a secondary response around the fuselage-tail junction.

The differences between the synchrophased and baseline configurations are presented in Figures 9(b) and (d). Looking at the front propeller plane (AF), small differences around the wing are observed with an average reduction value in this region of 3.4 dB. This is beneficial to the aircraft passengers and is driven by the propeller phase shift. Regions of reduced noise are captured at the extremes of the plane fore/aft of the aircraft and on the port/starboard sides. The projection of the acoustics waves $\sim 30^\circ$ aft of the outer front propellers results in an increase in the noise levels of between 10 and 20 dB. Although this contributes to an overall plane increase, it is again of benefit to the passengers as higher noise levels are projected away from the cabin.

In addition to these observations, which are seen on the rear plane (AR), the greatest reduction is seen between the two rear propellers. Here, a reduction upwards of 15 dB is observed. This is beneficial to the overall acoustic footprint as the higher noise level region generated around the fuselage-tail junction is significantly reduced.

Presented in Figure 10 is the averaged overall sound pressure level for the synchrophased configuration and the difference between the two configurations on the VF and VR planes. Focusing on the averaged synchrophased solutions, for both front (VF) and rear (VR) planes the majority of the medium level noise is directed above the aircraft. The acoustics waves either side of the front propellers, present in plane AF, is shown to have a vertical projection in plane VF. As a result, this is seen to be the dominant noise front away from the aircraft in terms of the size and noise level. Underneath the front plane (VF), the medium level noise is contained to within the aircraft span length. For the plane VR (Figure 10(c)), the medium level noise is projected across the entire

upper half of the plane over several wave bands.

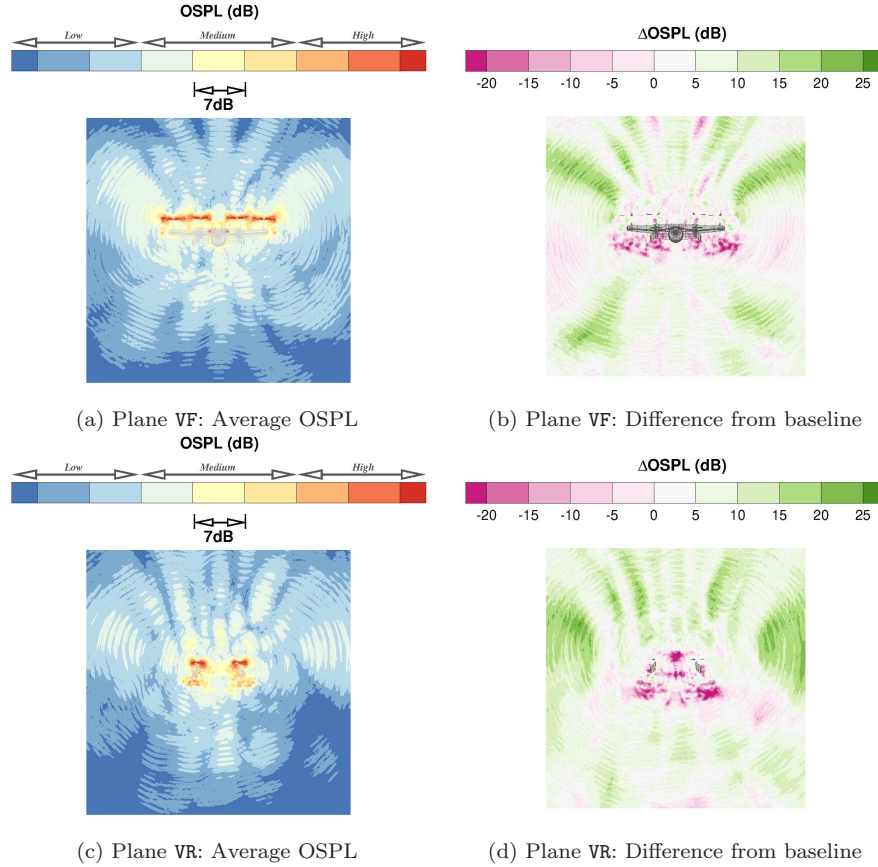


Figure 10: The average overall sound pressure level (OSPL) for the synchrophased configuration with the difference between the two configurations for the visualisation slices VF and VR in hover

In terms of the difference between the synchrophased and baseline configurations for both VF and VR planes (presented in Figures 10(b) & (d)), similar profiles as planes AF and AR are observed. A reduction in noise level is captured around the aircraft with the dominant regions being underneath the front wing and between the two rear propellers. These reductions range between 10 to 20 dB. The vertical projection of the acoustic waves outside of the front propellers results in an increase in noise levels either side of the aircraft on both planes.

Presented in Figure 11 is the average OSPL on the ground plane for the synchrophased configuration and the difference between the baseline result (Figure 7(a)). With the difference in overall sound pressure level contours kept constant as the planes around the aircraft (AF, AR, VF, VR), very little difference between the two configurations can be seen, hence line contours of $\pm 5dB$ are introduced to highlight certain regions. The high frequency oscillations in OSPL remain with the introduction of the synchrophasing phase shift. Certain pockets of small oscillations in noise level are found and these are contained to the very edge of the ground plane. On average the OSPL increases by $0.2dB$ across the entire plane.

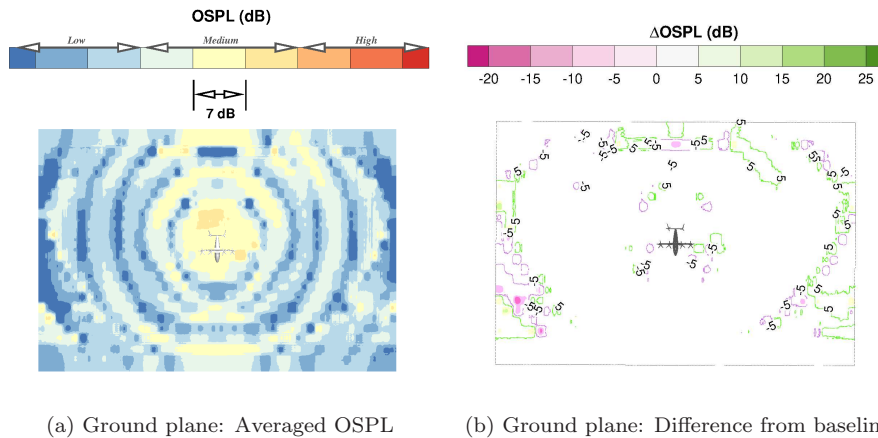


Figure 11: The average overall sound pressure level (OSPL) for the synchrophased configuration with the difference between the two configurations for the ground plane in hover

Presented in Figure 12 is the average surface OSPL for both simulated configurations. As observed from the baseline configuration (Figure 12(a)), the high level noise regions are contained around the propeller blades, fuselage-wing and fuselage-tail junctions. With the introduction of the phase shift (Figure 12(b)), significant alterations are found. The acoustics waves generated around the fuselage-tail junction have been significantly damped with the highest level of noise around the tail contained to the horizontal leading edge. Additionally,

the noise fluctuations across the fuselage cabin area have been mitigated with a smoother profile.

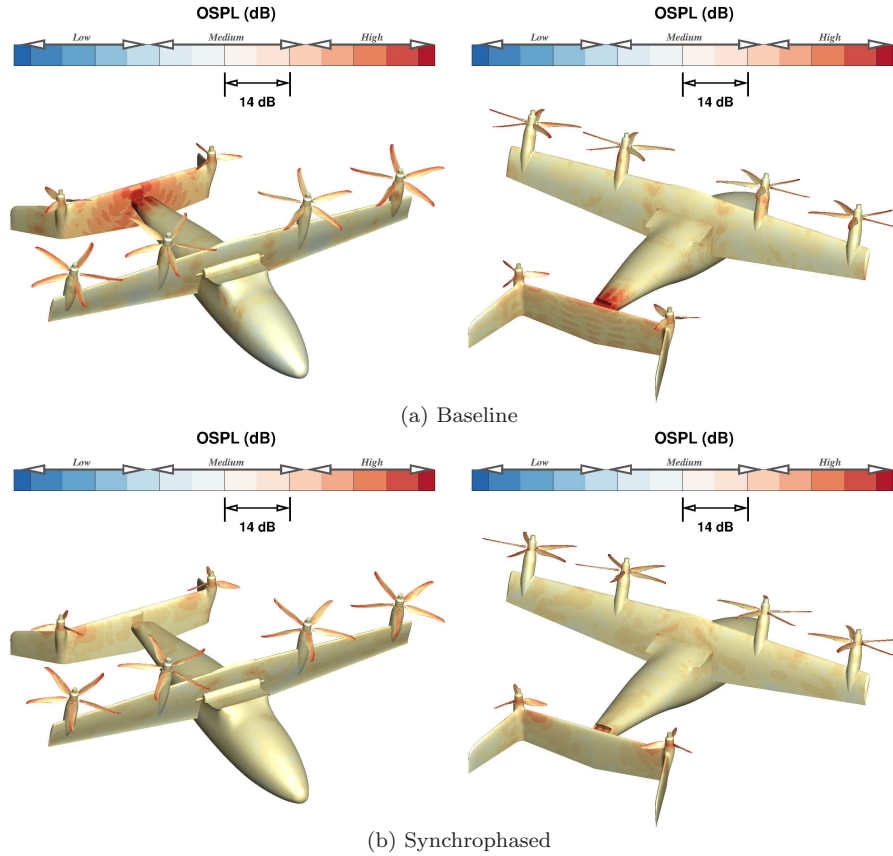


Figure 12: Comparison of the averaged surface OSPL between the synchrophased and baseline configurations visualised from the aircraft rear in hover

Looking at the average OSPL across certain sections of the aircraft gains insight into the greatest benefits. On average across the full aircraft a reduction in OSPL of $1dB$ is seen. Although this is small, the greatest changes comes from the maximum and minimum values. These both reduce by $8.8dB$ and $12.9dB$, respectively. This is driven by the reduction in tail noise fluctuations with an average reduction of $7.4dB$ across the full tail due to the synchrophased setup.

Looking closer at the key regions around the aircraft, slices around the fuse-

lage cabin and tail are taken for both configurations with a comparison presented in Figures 13 & 14, respectively, with the differences also presented. For the fuselage slice (Figure 13), peaks of increased noise are observed around the fuselage azimuth for the synchrophased configuration. These are seen at 270° , 315° and 90° . The majority of the curve indicates a reduction in noise levels, particularly around the starboard and port sides (0° & 180°). On average the synchrophased configuration reduces the noise levels outside of the cabin by $1.6dB$.

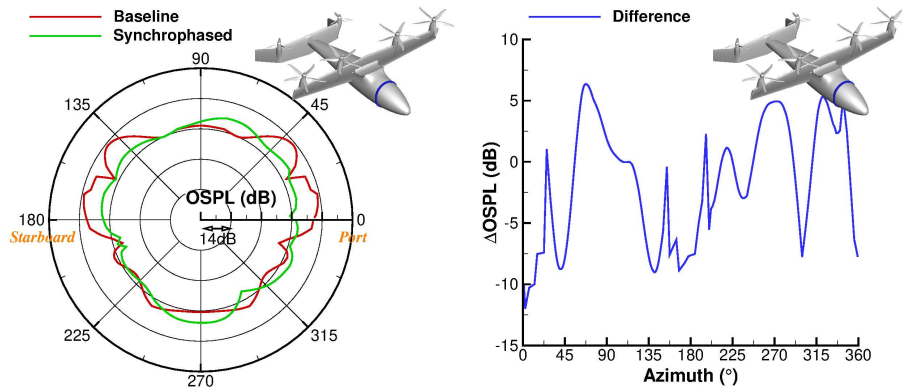


Figure 13: Comparison of the average surface OSPL between the synchrophased and baseline configurations at the fuselage cabin

For the tail slice, significant alterations are shown in Figure 14. The azimuth direction goes from leading edge at 0° to the trailing edge at 180° and then return to the leading edge at 360° . Due to the reduction in fuselage-tail junction oscillations, a reduction in average noise levels around the tail is seen. Large reduction peaks are observed at 135° and 225° with a plateau at $\sim 20dB$ across the remaining sections. On average at this centre tail slice, the noise level reduces by $24.2dB$.

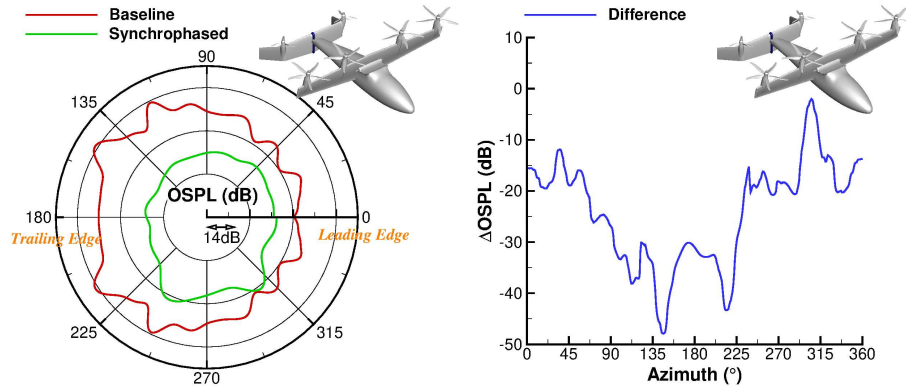


Figure 14: Comparison of the average surface OSPL between the synchrophased and baseline configurations at the aircraft tail

4.2. Results of the Synchrophased Aircraft in Forward Flight

Presented in Figure 15 is the averaged OSPL for the synchrophased configuration on slices AR and VR along with the difference between this and the baseline configuration. Focusing on the averaged result for slice AR (Figure 15(a)), a similar profile as the hover simulation (Figure 9(c)) is found at the rear. The highest noise levels are contained within the propeller blade radius. However, due to the reduction in the number of propellers from hover to forward flight, the near-field noise levels reduce to lower values around the aircraft. Higher frequency oscillations are observed at the fuselage-tail junction. These waves are dissipated due to the influence of the freestream velocity and balancing of the port/starboard propeller acoustic waves. The differences between the synchrophased and baseline configurations for slice AR (Figure 15(b)) are smaller compared to the hover flight condition. The differences are mainly contained to the starboard side with reductions of between 5 to 10 dB seen between the two rear propellers, around the wing tip and above the aircraft towards the slice edge. The reduction between the two rear propellers is a result of the phase differences introduced between the port and starboard propellers. The reductions around the wing tip and towards the slice edge are a result of the acoustic waves

being projected further outboards of the aircraft due to the phase difference.

For the horizontal slice (Figure 15(c)), it is observed that slightly higher noise levels are found along the horizontal plane, **VR**, as compared to the vertical, **AR**, thus indicating that the rear propeller acoustic waves are projected further along the horizontal direction than the vertical. This is potentially beneficial for any ground plane observer. Although such noise levels are found to be higher, they are still significantly lower than what is observed in hover (Figure 10(c)). Due to the introduction of the phase shift, slightly higher levels of noise are found on the synchrophased starboard side and this is shown in Figure 15(d). The change in starting position of the acoustic waves results in a mis-match between the baseline and synchrophased peaks-troughs, and therefore slightly reduces the benefits.

Presented in Figure 16 is the averaged OSPL along the fictitious ground plane for the synchrophased configuration in forward flight and the difference between the baseline and synchrophased configurations. As observed from the baseline simulations (Figure 7) with a comparison to the hover synchrophased simulation (Figure 11), higher noise levels are obtained along the ground plane for the aircraft in forward flight. Despite this increase, the high frequency fluctuations observed in hover are mitigated and this is seen as beneficial to any ground observer. Additionally, due to the forward flight speed, the ground observer is likely to be in contact with the higher value noise level for a short period of time in comparison to the hover condition.

In a similar manner to the hover simulation, very small changes are observed between the synchrophased and baseline configuration in forward flight. Slightly higher reductions of $\sim 2dB$ are observed around the starboard side, and this again mirrors the solution seen on the near-field visualisation planes. An average reduction of $2dB$ is observed across the ground plane in forward flight.

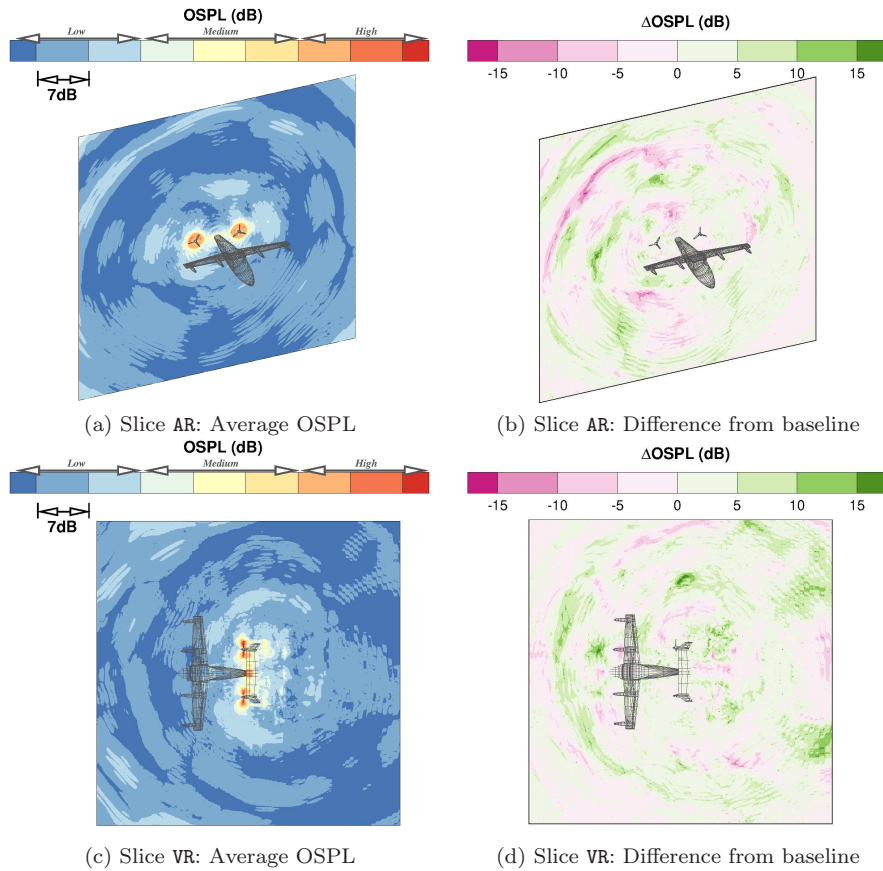


Figure 15: Average synchrophased OSPL and the difference in OSPL between the synchrophased and baseline configurations for the axial (AR) and horizontal (VR) slices

Presented in Figure 17 is the averaged surface overall sound pressure level for both the baseline and synchrophased configurations. Very similar profiles are found between the two configurations with the higher value noise levels contained towards the rear and medium/low levels across the fuselage. In terms of average values across the full aircraft, the introduction of the synchrophasing reduced the noise level by $\sim 1dB$. Although this is small in terms of the average, pockets of higher reductions can be seen across the aircraft. Focusing on the tail horizontal stabiliser, high noise levels are contained to the leading edge with smaller pockets of high-medium levels seen along the chord for the baseline

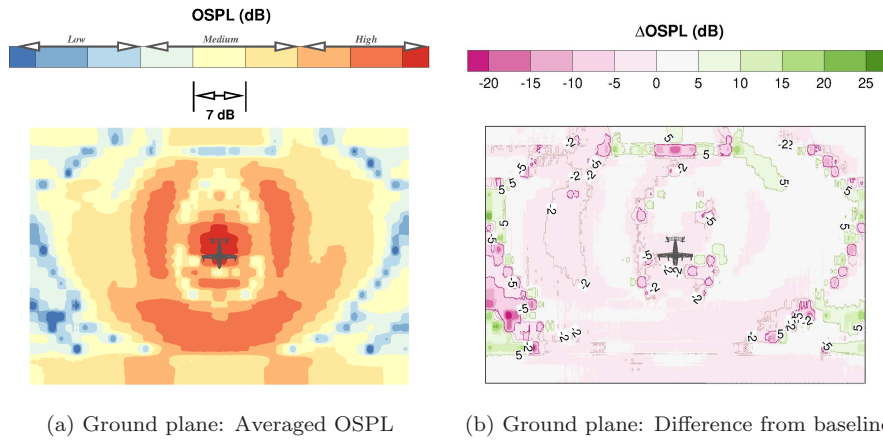


Figure 16: Averaged OSPL for the ground flow-field probes for the synchrophased configuration in forward flight

simulation. For the synchrophased configuration, a similar profile is found on the port side with a pocket of lower value noise seen on the starboard. This is again a consequence of the balancing of the acoustic waves between the two propellers.

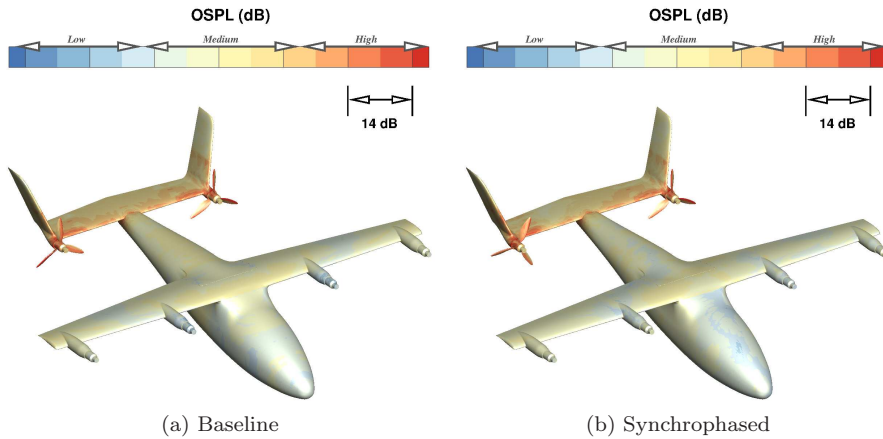


Figure 17: Comparison of the averaged surface OSPL between the synchrophased and baseline configurations

Presented in Figure 18 is the comparison of the surface averaged OSPL between the synchrophased and baseline configurations at the fuselage cabin. In terms of average values and mirroring the full aircraft surface, a slightly lower

value of OSPL is seen with the synchrophased configuration with a reduction of $\sim 1dB$. Around the fuselage azimuth, the difference in OSPL oscillates between the two configurations. At the starboard and port sides (0° and 180° , respectively), a slight increase in OSPL is seen for the synchrophasing. This equates to a maximum difference of $\sim 7dB$ and $\sim 5dB$ on the port and starboard sides, respectively. The opposite is found around the top and starboard lower section. Here, reductions of $\sim 10dB$ are seen. This is beneficial as the fuselage cabin design contains a re-enforced glass-like structure along the upper half. As a result, very little mitigation of the noise level between the outside surface and inside cabin can be introduced. If such a mitigation is conducted via the synchrophasing of the propellers, an improvement in the cabin noise comfort can be found. In a similar manner, the structure on the starboard/port sides can be re-enforced and therefore the increase in surface noise due to the synchrophasing can be mitigated for the passengers.

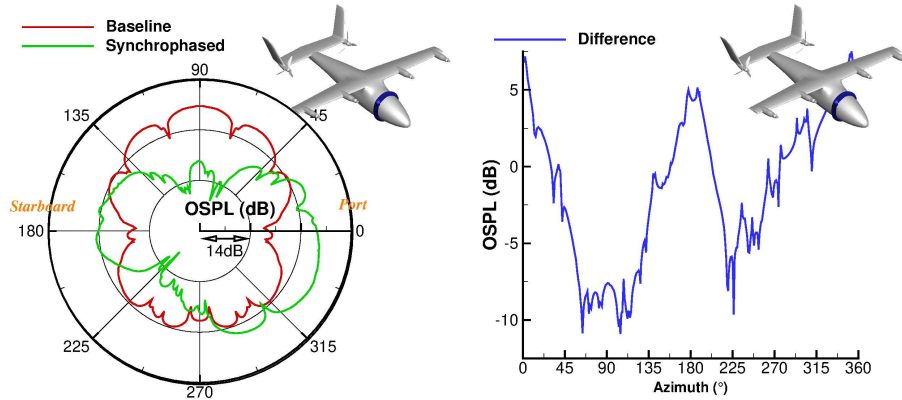


Figure 18: Comparison of the average non-dimensional surface OSPL between the synchrophased and baseline configurations at the fuselage cabin

5. Conclusions

The following conclusions are observed from the baseline configuration simulations in hover and forward flight:

- The combination of rotating wing and tail components combined with the multi-rotor design requires a key focus on the grid and simulation setup. For this investigation, the chimera method was utilised and proved to be effective in capturing the key acoustic findings.
- It is clear from the baseline configurations that the hover flight condition is more critical in terms of the acoustics levels compared to forward flight. The use of the front propellers for vertical take-off significantly amplifies the noise levels around the fuselage cabin. Not only are higher levels of acoustics seen on the aircraft surface, the flow-field slices indicate a propagation of noise further outwards of the vehicle.
- The introduction of synchrophasing to the aircraft found an altering in the sound pattern and thus seeing a reduction in sound levels across the aircraft surface but, more importantly, near the cockpit. Pockets of reduced noise levels were captured in the near-field region with such reductions minimal as the acoustic waves reach the ground plane.
- It is critical to note that the study of propeller synchrophasing was a binary test to determine if benefits to the overall noise levels can be seen. This was observed across the surface for the given angles, with the selected angles not optimised for acoustics. Further optimisation is advised to be conducted on-board the aircraft with an installed synchrophase system. The use of electric motors can allow phase shifts to be conducted easily, thus allowing multiple configurations to be tested at a given instance and the phasing of the blades to be changed during flight.
- Further improvements to the overall noise level can be obtained via more complex optimisation strategies. These include the alteration of the propeller blade shape and possibly the introduction of ducts.

6. Acknowledgments

The authors would like to thank Roll-Royce for their support and permission to publish the work. Special mention to Anmol Manohar and Dave Fillingham for their technical support. This work used the Cirrus UK National Tier-2 HPC Service at EPCC (<https://www.epcc.ed.ac.uk/cirrus>) funded by the University of Edinburgh and EPSRC (EP/P020267/1) under project number EC004. Results were obtained using the ARCHIE-WeSt High Performance Computer (<http://www.archie-west.ac.uk/>) based at the University of Strathclyde.

References

- [1] W. Ng, A. Datta, Hydrogen fuel cells and batteries for electric-vertical takeoff and landing aircraft, *Journal of Aircraft* 56 (5) (2019) 1765–1782, doi: 10.2514/1.C035218.
- [2] R. Whittle, The demand for on-demand mobility, *Vertiflite* January/February (2017) 34–38.
- [3] Rolls-royce unveils 'flying taxi' at farnborough airshow, <https://www.cityam.com/rolls-royce-unveils-flying-taxi-farnborough-airshow/>, last accessed 26th June 2020 (2018).
- [4] Rolls-royce unveils evtol air taxi concept at farnborough airshow, <https://www.theengineer.co.uk/rolls-royce-evtol-air-taxi/>, last accessed 26th June 2020 (2018).
- [5] P. Arguelles, M. Bischoff, P. Busquin, B. Droste, S. R. Evans, W. Kroll, J. Lagardere, A. Lina, J. Lumsden, D. Ranque, S. Rasmussen, P. Reutlinger, S. R. Robins, H. Terho, A. Wittlov, *European aeronautics: A vision*

- for 2020: Meeting society's needs and winning global leadership, Tech. rep., European Commission (2001).
- [6] T. M. Darecki, C. Edelstenne, T. Enders, E. Fernandez, P. H. J. Herteman, M. Kerkloh, I. King, P. Ky, M. Mathieu, G. Orsi, G. Schotman, C. Smith, J. Worner, Flightpath 2050: Europe's vision for aviation. report of the high level group on aviation research, Tech. rep., ACARE (Advisory Council for Aeronautics Research in Europe) (2011).
- [7] B. Magliozzi, Generalized propeller noise estimating procedure - revision d, Tech. rep., Hamilton Standard Publication (1971).
- [8] M. Smith, A prediction procedure for propeller aircraft flyover noise based on empirical data, Tech. Rep. 810604, SAE International (1981).
- [9] W. Dobrzynski, A general prediction procedure for light propeller driven aeroplane flyover noise signatures, in: Proceedings of Inter-Noise 94: Noise - Quantity and Quality, 1994.
- [10] H. Si, T. Wang, Grid-optimized upwind dispersion-relation-preserving scheme on non-uniform cartesian grids for computational aeroacoustics, *Aerospace Science and Technology* 12 (8) (2008) 608–617, doi: 10.1016/j.ast.2008.02.003.
- [11] A. J. Garcia, G. Barakos, Assessment of a high-order muscl method for rotor flows, *International Journal for Numerical Methods in Fluids* 87 (6) (2018) 292–327, doi: 10.1002/flid.4492.
- [12] Y. Jin, F. Liao, J. Cai, P. Morris, Investigation on rod-airfoil noise with high-order cell-centered finite difference method and acoustic analogy, *Aerospace Science and Technology* 102 (2020) 105851, doi: 10.1016/j.ast.2020.105851.

- [13] I. Shahin, M. Alqaradawi, M. Gadala, O. Badr, On the aero acoustic and internal flows structure in a centrifugal compressor with hub side cavity operating at off design condition, *Aerospace Science and Technology* 60 (2016) 68–83, dOI: 10.1016/j.ast.2016.10.031.
- [14] S. Sharma, J. Garcia-Tiscar, J. Allport, S. Barrans, A. Nickson, Evaluation of modelling parameters for computing flow-induced noise in a small high-speed centrifugal compressor, *Aerospace Science and Technology* 98 (2020) 105697, dOI: 10.1016/j.ast.2020.105697.
- [15] S. Zhong, X. Zhang, J. Gill, R. Fattah, Y. Sun, Geometry effect on the airfoil-gust interaction noise in transonic flows, *Aerospace Science and Technology* 92 (2019) 181–191, dOI: 10.1016/j.ast.2019.06.006.
- [16] S. Vourous, I. Goulos, V. Pachidis, Integrated methodology for the prediction of helicopter rotor noise at mission level, *Aerospace Science and Technology* 89 (2019) 136–149, dOI: 10.1016/j.ast.2019.03.061.
- [17] P. Beaumier, Y. Delrieux, Description and validation of the onera computational method for the prediction of blade-vortex interaction noise, *Aerospace Science and Technology* 9 (1) (2005) 31–43, dOI: 10.1016/j.ast.2004.07.008.
- [18] F. Dehaeze, G. Barakos, Mesh deformation method for rotor flows, *Journal of Aircraft* 49 (1) (2012) 82–92, dOI: 10.2514/1.C031251.
- [19] G. Chirico, G. Barakos, N. Bown, Numerical aeroacoustic analysis of propeller designs, *The Aeronautical Journal* 122 (1248) (2018) 283–315, dOI: 10.1017/aer.2017.123.
- [20] C. Crozon, R. Steijl, G. Barakos, Coupled flight dynamics and cfd - demon-

- stration for helicopters in shipborne environment, *The Aeronautical Journal* 122 (1247) (2018) 42–82, dOI: 10.1017/aer.2017.112.
- [21] S. Babu, G. Loupy, F. Dehaeze, G. Barakos, N. Taylor, Aeroelastic simulations of stores in weapon bays using detached-eddy simulation, *Journal of Fluids and Structures* 66 (2016) 207–228, dOI: 10.1016/j.jfluidstructs.2016.07.014.
- [22] D. Wilcox, Multiscale model for turbulent flows, *AIAA Journal* 26 (11), dOI: 10.2514/3.10042.
- [23] N. Scrase, M. Maina, The Evaluation of Propeller Aero-acoustic Design Methods by Means of Scaled-Model Testing Employing Pressure Tapped Blades and Spinner, in: 19th ICAS Congress, Anaheim, California, USA., International Council of the Aeronautical Sciences, 1994, iSBN: 1563470845.
- [24] A. Gomariz-Sancha, M. Maina, A. Peace, Analysis of propeller-airframe interaction effects through a combined numerical simulation and wind-tunnel testing approach, in: 53rd AIAA Aerospace Sciences Meeting, AIAA, Kissimmee, Florida, 2015, dOI: 10.2514/6.2015-1026.
- [25] A. Knepper, N. Bown, IMPACTA Wind-tunnel Instrumentation Specification, Tech. Rep. ITS 01777, Issue 3, Dowty Propellers (GE Aviation Systems Ltd) (2014).
- [26] A. Zarev, R. Green, Experimental investigation of the effect of yaw angle on the inflow of a two-bladed propeller, *Aerospace Science and Technology* 103 (2020) 105940, dOI: 10.1016/j.ast.2020.105940.
- [27] G. Barakos, C. Johnson, Acoustic comparison of propellers, In-

- ternational Journal of Aeroacoustics 15 (6-7) (2016) 575–594, doi: 10.1177/1475472X16659214.
- [28] R. Higgins, A. Jimenez-Garcia, G. Barakos, N. Bown, High-fidelity computational fluid dynamics methods for the simulation of propeller stall flutter, AIAA Journal 57 (12) (2019) 52815292, doi: 10.2514/1.J058463.
- [29] R. Higgins, G. Barakos, E. Jinks, Estimation of three-dimensional aerodynamic damping using cfd, The Aeronautical Journal 124 (1271) (2019) 24–43, doi: 10.1017/aer.2019.135.
- [30] R. Higgins, A. Zarev, G. Barakos, R. Green, Numerical investigation of a two-bladed propeller inflow at yaw, Journal of Aircraft 57 (2) (2020) 292304, doi: 10.2514/1.C035647.
- [31] A. Jimenez-Garcia, G. Barakos, Numerical simulations on the erica tiltrotor, Aerospace Science and Technology 64 (2017) 171–191, doi: 10.1016/j.ast.2017.01.023.
- [32] A. Jimenez-Garcia, G. Barakos, S. Gates, Tiltrotor cfd part i - validation, The Aeronautical Journal 121 (1239) (2017) 577–610, doi: 10.1017/aer.2017.17.
- [33] M. Jarkowski, M. Woodgate, G. Barakos, J. Rokicki, Towards Consistent Hybrid Overset Mesh Methods for Rotorcraft CFD, International Journal for Numerical Methods in Fluids 74 (8) (2014) 543–576, doi:10.1002/fld.3861.
- [34] G. Chirico, G. Barakos, N. Bown, Propeller installation effects on turbo-prop aircraft acoustics, Journal of Sound and Vibration 424 (2018) 238–262, doi: 10.1016/j.jsv.2018.03.003.

- [35] D. Han, V. Pastrikakis, G. Barakos, Helicopter flight performance improvement by dynamic blade twist, *Aerospace Science and Technology* 58 (2016) 445–452, dOI: 10.1016/j.ast.2016.09.013.
- [36] D. Han, K. Yang, G. Barakos, Extendable chord for improved helicopter rotor performance, *Aerospace Science and Technology* 80 (2018) 445–451, dOI: 10.1016/j.ast.2018.07.031.
- [37] D. Han, C. Dong, G. Barakos, Performance improvement of variable speed rotors by gurney flaps, *Aerospace Science and Technology* 81 (2018) 118–127, dOI: 10.1016/j.ast.2018.07.044.
- [38] J. Riemenschneider, S. Opitz, Measurement of twist deflection in active twist rotor, *Aerospace Science and Technology* 15 (3) (2011) 216–223, dOI: 10.1016/j.ast.2010.12.008.
- [39] A. Batrakov, A. Kusyumov, S. Mikhailov, G. Barakos, Aerodynamic optimization of helicopter rear fuselage, *Aerospace Science and Technology* 77 (2018) 704–712, dOI: 10.1016/j.ast.2018.03.046.